Anti-Hertz bulging of actuated liquid crystal elastomers

L. Angela Mihai [a], Alexandra Gablier [b], Eugene M. Terentjev [b], Alain Goriely [c],*

[a] School of Mathematics, Cardiff University, Cardiff, UK
[b] Cavendish Laboratory, University of Cambridge, Cambridge, UK
[c] Mathematical Institute, University of Oxford, Oxford, UK

ARTICLE INFO

ABSTRACT

We consider the 'anti-Hertz' elastic problem of inverse indentation, which happens when the surface of an elastic material is pressed down with a plate with a round hole to form a bulge. This classical problem takes on a new life when a polydomain nematic liquid crystal elastomer is used. In this case, the nematic director aligns with the leading principal direction of local stress distribution created by bulging. When the deformed material is crosslinked a second time, this alignment pattern and the resulting permanent protrusion are preserved as pressure is removed, creating a bulge that can be reversibly actuated from a flat surface upon cooling. Experimentally, we also observe a dimple ring around the bulge and a punt (indentation) underneath it at the bottom. Theoretically, we model the deformation by coupling linear elastic and anelastic deformations using non-monotonic nematic elasticity and the singular stress-order relation of the polydomain-monodomain transition. The theory is in excellent agreement with the experiments, and predicts the emergence of all observed features.

Liquid crystal elastomers (LCEs) have emerged in the last decade as promising multifunctional active materials. They are formed of cross-linked polymeric chains with embedded mesogenic molecules and can display both elastic and nematic (or other mesophase) behavior, the latter order changing in response to external stimuli such as heat, light, and mechanical stress [1]. This makes them the material of choice for several important applications of mechanical actuation [2], including in biomedical engineering, power generation and flexible electronics.

Here, we explore the possibility of LCEs to form small bumps on the surface of a sheet that can be further programmed. The main idea is to provide the correct combined mechanical stress and heat profile to create an array of such bumps. The fine control of this process could lead to dynamic tactile displays or refreshable LCE screens containing Braille character cells [3]. Since the actuation of these bumps is reversible, repeatable, and re-programmable, this process may be suitable for further technological development.

The problem of bump formation is also of outstanding interest from a purely physical point of view. The Hertz problem in contact mechanics consists of computing the deformations and stresses of two elastic bodies with curved surfaces pressed against each other [4,5]. It is one of the most important problems of elasticity, and is the process behind force microscopy, friction, and all indentation techniques. We refer to the formation of a bulge as the *anti-Hertz problem*, since the boundary conditions are inverted. Rather than having a displacement prescribed in a localized region where contact takes place surrounded by a large planar stress-free region, in bulging we have a central opening that is stress-free, surrounded by a large planar domain with prescribed displacement, Fig. 1(a). A solution of this problem has been proposed within the framework of linear isotropic elasticity with applications to the bulging of brain tissue following decompressive craniectomy [6–8].

The elastic bulging is fully reversible and by itself insufficient to describe the permanent deformations found in LCEs. Indeed, in polydomain nematic LCE, the mesogens are separated into misaligned regions of 1-2 μm size [9], such that in every domain they are aligned along a local director, but the overall response is isotropic [10–12]. The uniformly aligned nematic monodomain structure can form from polydomain LCE through stretching during the final cross-linking of the polymer network, or by cooling from the isotropic to a nematic phase under an external stress field [13–15]. In this case, the additional anelastic behavior determined by the local nematic order evolves during the formation of a bump and changes dramatically the bulging problem leading to a permanent bump with a different morphology, followed by its reversible thermal actuation. Here, we study this problem experimentally and theoretically.

* Corresponding author.
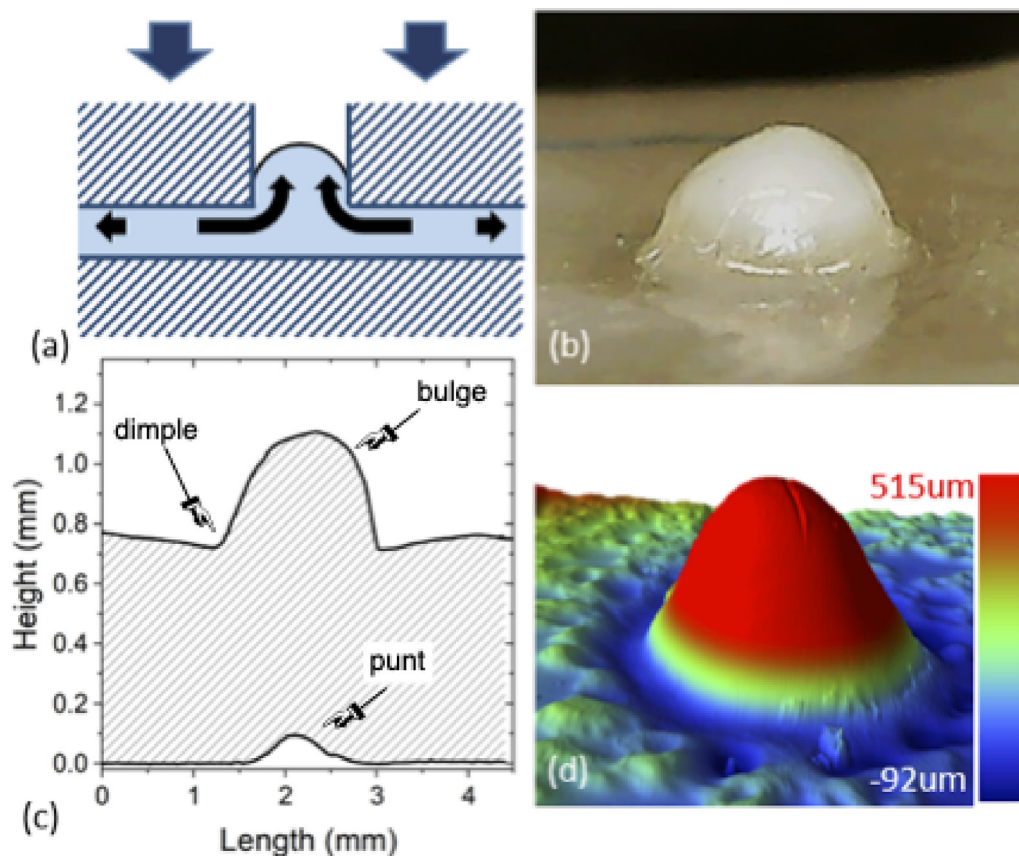 E-mail address: goriely@maths.ox.ac.uk (A. Goriely).

Fig. 1. (a) The sketch illustrating the pressurized bulge in an isotropic linear elastic material; (b) The photo of our free-standing bulge, in ambient conditions (at maximum nematic oder); (c) The line scan of the top and bottom surfaces of the LCE layer, giving detailed information on height distribution around and underneath the bulge; (d) The profilometer map of the local height around the bulge.

1. Methods

1.1. Experiment

To produce an experimental illustration of the anti-Hertz bulge, we follow the work on Braille actuators [3] and use a main-chain nematic LCE based on the thiol-acrylate click chemistry and flexible crosslinkers. It is the system of choice due to its robust and reproducible production and properties (see [16–18] for details on material synthesis). We start with a polydomain nematic elastomer of isotropic genesis, partially crosslinked. For this, upon cooling, the isotropic crosslinked network enters into the nematic phase with a set of quenched random crosslinks, but no additional texture constraints [10]. In addition, when during crosslinking this network is swollen by a solvent, the stretched chains fold on de-swelling without entangling (i.e. additional internal constraints) [19]. This is our starting flat polydomain LCE layer.

An important factor is the ability to "freeze" the pressurized bulge, and its pattern of induced local order, by the second-step (final) crosslinking, see [3] for detail. The half-crosslinked elastomer layer was sandwiched between a flat support and a flat teflon plate with holes of the desired dimension and shape. The sandwich was introduced in a hot press at room temperature, and a set pressure of under 10 kPa was applied to form the bulge. The pressurized film was then heated to complete the second crosslinking in the isotropic phase, which preserved the pattern of local stress and induced nematic order in the bulge on subsequent cooling.

After releasing the pressure and annealing the load-free elastomer, we cooled it down to the nematic phase to recover the permanently 'recorded' bulge driven by a pattern of local uniaxial order and the associated local extension, as illustrated in Fig. 1. The surface topography was measured by the DektakXT profilometer from Bruker to obtain line scans and surface map profiles. Fig. 1(c) shows the combined line scan of both the top and the bottom surface of the LCE layer, showing that, in addition to the prominent *bulge*, there is a matching indentation underneath, the *punt*, where the material was displaced to supply the protrusion. One can also see *dimples* forming around the protrusion rim, again to supply material into the growing bulge, since the material volume is conserved.

1.2. Theory

We model the deformation of the polydomain LCE layer pressed between two horizontal rigid plates when the top plate contains a circular opening with straight edge and the other acts as a fixed support. Locally, the material undergoes different degrees of the polydomain-monodomain transition along the local axes of principal stresses, mimicking the polydomain–monodomain transition under uniaxial tensile stress, well-studied experimentally and theoretically. Specifically, we use the model for the uniaxial order parameter as a function of stress [15], at every point in space:

$$Q(\sigma) \approx Q_{\max}(T) \exp\left[-c_1 / \sqrt{(\sigma_+ - \sigma_-) - c_0}\right], \tag{1}$$

where $Q_{\max}(T)$ is the temperature-dependent intrinsic value of nematic order parameter, before its macroscopic average reduction due to misaligned domains [20], $\sigma_{\pm}$ are the principal stress components, c_0 is the 'plateau stress' value, and the material constant c_1 is determined by the ratio of the Frank elastic modulus of
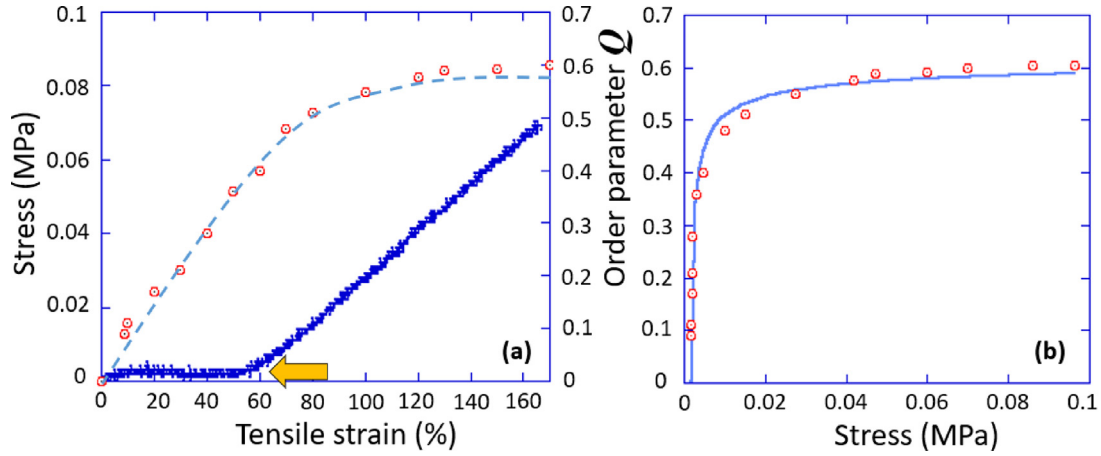
Fig. 2. (a) The stress–strain curve of polydomain–monodomain transition in our LCE, overlaid with the values of induced order parameter Q reported on the second vertical axis. The arrow marks the soft stress plateau c_0, where the alignment of domains takes place. (b) The same data for order parameter Q is plotted against stress, with the line representing best fit with Eq. (1).

the underlying nematic and the degree of quenched disorder in the crosslinked network [15]. Since the rate of pressure was small in our experiments, and in practice the quasi-equilibrium stress plateau of the ideal isotropic-genesis polydomain–monodomain transition is almost zero, we neglect the small 'jump' of Q at the critical point [12,21].

Fig. 2 illustrates these parameters in our experimental system. The plot in Fig. 2(a) shows the classical stress–strain curve of polydomain-monodomain transition, where the arrow points at the soft stress plateau [12,15] of $c_0 = 0.0018$ MPa, and the values of induced order parameter Q (determined by X-ray scattering) at several points in strain. The plot in Fig. 2(b) contains the same values Q plotted against the stress, and fitted by Eq. (1) with $Q_{max} = 0.63$ and $c_1 = 0.019$. We will use these parameters for the induced order $Q(\sigma)$ in the analysis below.

An important feature of the system is the combination of elastic and anelastic effects that can be captured through a multiplicative decomposition of the deformation gradient [22] such that the deformation gradient **F** with respect to the reference polydomain configuration takes the form [23,24]

$$\mathbf{F} = \mathbf{G} \cdot \mathbf{A}, \tag{2}$$

where **A** is the *local elastic deformation tensor*, and **G** is the *natural deformation tensor* from the isotropic to a nematic state. Local mass conservation implies that during the anelastic remodeling we have $\det \mathbf{G} = 1$.

Following [24], the natural deformation tensor can be written as follows

$$\mathbf{G} = a^{-1/6}\mathbf{I} + \left(a^{1/3} - a^{-1/6}\right) \mathbf{n} \otimes \mathbf{n}, \tag{3}$$

where $\mathbf{n} = [\cos\theta, \sin\theta, 0]^T$ is the local nematic director in the current axisymmetric configuration and $a = (1 + 2Q)/(1 - Q)$ is the chain anisotropy parameter [25].

2. Results

2.1. The local elastic deformation tensor

The bulging of a homogeneous isotropic elastic material under uniform applied pressure can be adequately captured by linear elasticity [6–8]. Hence, we write $\mathbf{A} = \nabla\mathbf{u} + \mathbf{I}$, where **u** is the displacement field from the reference configuration to the elastic deformed state and **I** is the identity tensor.

The stress tensor for an unconstrained isotropic linear elastic material is given by

$$\sigma = \frac{E}{1 + \nu}\mathbf{e} + \frac{E\nu}{(1 + \nu)(1 - 2\nu)} (\operatorname{tr} \mathbf{e}) \mathbf{I}, \tag{4}$$

where E is the Young modulus, ν is Poisson's ratio, and $\mathbf{e} = \left(\nabla\mathbf{u} + \nabla\mathbf{u}^T\right)/2$ is the infinitesimal strain tensor.

We assume an axisymmetric deformation, with x as the horizontal radial direction and z the vertical direction; in both cases, the distances are non-dimensional, scaled by the radius of the hole. When the material is incompressible ($\nu = 1/2$, see [26] for discussion) and the gap has a straight edge while the applied pressure is constant, setting the layer's top surface at $z = 0$, the components of the displacement field at this surface take the form [8]:

$$u_x = 0, \qquad u_z = \delta - \frac{3p_0}{2E}\sqrt{1 - x^2}, \tag{5}$$

where δ is a uniform vertical displacement and p_0 is the applied pressure. The area of the bulge is $A_b = \pi h/2$, where $h = 3p_0/2E$ is the height.

With rounded edges, the solution away from the edge is well captured by the straight-edge case but has the advantage to reduce the local stress singularity created by the jump [8]. Hence it may prevent material failure at that point. Since the deformation and stress profiles are almost indistinguishable away from the edge, and the experiments are carried out with straight edges, the simpler straight-edge solution is sufficient for our analysis.

In the deformed layer, the components of the linear elastic stress tensor for $x \geq 0$ and $z \geq 0$ have the following explicit forms [8]:

$$\sigma_{xx} = -\frac{p_0}{\rho\sqrt{2}}\left[\left(x - \frac{z\zeta}{\rho^2}\right)\sqrt{\rho - \xi} + z\left(1 + \frac{\xi}{\rho^2}\right)\sqrt{\rho + \xi}\right]$$

$$\sigma_{zz} = -\frac{p_0}{\rho\sqrt{2}}\left[\left(x + \frac{z\zeta}{\rho^2}\right)\sqrt{\rho - \xi} + z\left(1 - \frac{\xi}{\rho^2}\right)\sqrt{\rho + \xi}\right]$$

$$\sigma_{xz} = \frac{p_0}{\rho\sqrt{2}}\frac{z}{\rho^3}\left(\xi\sqrt{\rho - \xi} + \zeta\sqrt{\rho + \xi}\right),$$

where $\xi = 1 - x^2 + z^2$, $\zeta = 2x$ and $\rho = \sqrt{\xi^2 + \zeta^2}$. The small strain components are

$$e_{xx} = (2\sigma_{xx} - \sigma_{zz})/2E,$$
$$e_{zz} = (2\sigma_{zz} - \sigma_{xx})/2E,$$
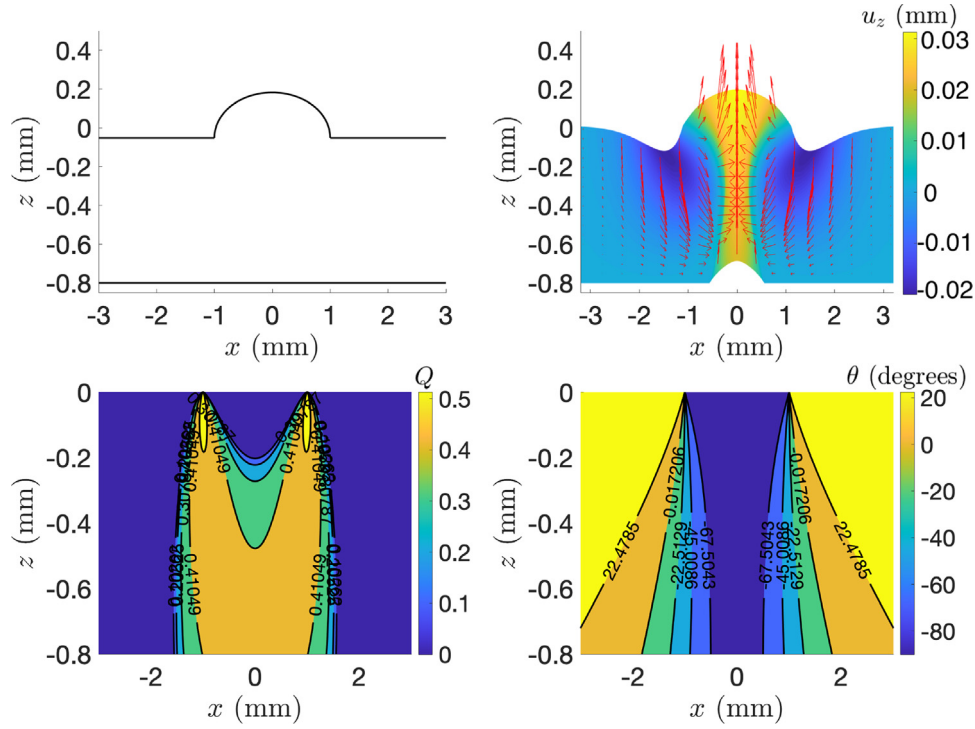$$e_{xz} = 3\sigma_{xz}/2E.$$

Fig. 3. (a) Analytical deformation profile of the pressurized LCE layer when $E = 32$ kPa and $p_0 = 5$ kPa; (b) Finite element simulation of the naturally deformed LCE layer when $Q_{max} = 0.65$, with arrows indicating local deformation and colors showing vertical displacement; (c) The distribution of the uniaxial order parameter Q in the pressurized layer, below the bulge; (d) The distribution of the angle θ for the orientation of the nematic director in the pressurized layer, below the bulge.

As the elastic material deforms, the nematic molecules reorient in the leading direction of the principal stress components

$$\sigma_\pm = \frac{1}{2}\left[\sigma_{xx} + \sigma_{zz} \pm \sqrt{(\sigma_{xx} - \sigma_{zz})^2 + 4\sigma_{xz}^2}\right], \qquad (6)$$

with principal strains $e_\pm = (\sigma_\pm - \sigma_\mp/2)/E$.

We define θ to be the polar angle of the director alignment w.r.t. the horizontal direction, from which we have

$$\sigma_{xx} = \sigma_+ \cos^2\theta + \sigma_- \sin^2\theta,$$
$$\sigma_{zz} = \sigma_+ \sin^2\theta + \sigma_- \cos^2\theta,$$
$$\sigma_{xz} = (\sigma_+ - \sigma_-)\sin\theta\cos\theta.$$

For $-1 < x < 1$ and $0 < z \ll 1$, we obtain $\sigma_+ \approx \sigma_{zz}$ and $\sigma_- \approx \sigma_{xx}$. Hence, $\theta \approx \pi/2$ and we conclude that the director aligns vertically in the emerging bulge.

Fig. 3(a) presents the profile of the pressurized LCE layer obtained from our analytical calculations with Young's modulus $E = 32$ kPa and applied pressure $p_0 = 5$ kPa. The director orientation and its nematic order in the pressurized bulge will be 'recorded' by the second crosslinking in order to be recovered when the unloaded material reacts spontaneously to temperature changes. Then, only Q_{max}, and hence the anisotropic parameter a, will vary with temperature, while the nematic director pattern **n** remains frozen. For visualization, Fig. 3(b) displays a finite element simulation of the naturally deformed LCE model when $Q_{max} = 0.65$. Contour plots of the order parameter Q in the pressurized layer are represented in Fig. 3(c). For the nematic director, contour plots of the orientation angle θ are shown in Fig. 3(d).

2.2. Actuation of the load-free bulge

In general, after loading and subsequent unloading, the nematic material does not return to its initial stress-free configuration, but exhibits a residual strain. The deformed pressurized

LCE layer contains a vertical bulge emerging through the gap in the top plate. After fixing the local map of induced nematic order **Q(x)** via the second crosslinking, and removing the applied load, a punt is formed below the bulge, at the interface of the load-free layer with the bottom plate, as well as the dimple around the bulge.

Figs. 4(a,b) illustrate the experimental results on the load-free bulge on heating the LCE into isotropic phase. This variation, from the protruded bulge to nearly-flat surface in the isotropic phase is caused by the change of underlying order parameter magnitude $Q_{max}(T)$, which can be measured independently [20].

Our theoretical model calculates the shape of the load-free spontaneously deformed layer, with different values of Q_{max}, as shown in Fig. 4(c) where the variation with temperature is reflected. For the naturally actuated bulge, using Eq. (2), the components of the displacement field at $z = 0$ take the following form as functions of the temperature-dependent anisotropy parameter $a(x)$,

$$\bar{u}_x = 0, \qquad \bar{u}_z = u_z \frac{a^{1/3} - 1}{a_0^{1/3} - 1}, \qquad (7)$$

where $u_z(x)$ is given by Eq. (5) and $a_0(x)$ is the anisotropy of new crosslink orientations. Hence these surface profiles are developed by the local director and order parameter in the bulge, which are depicted in Fig. 4(d). When the order decreases to zero in the isotropic phase, we recover the stress-free flat surface, as expected.

3. Discussion

We designed and implemented the actuation of a liquid crystal elastomer sheet that can be programmed to produce small bumps on a flat surface at different temperatures. The original polydomain LCE is capable of large reversible deformations and forms bulges when pressed down trough round holes under a perforated plate. Such a deformation induces in the material a nematic
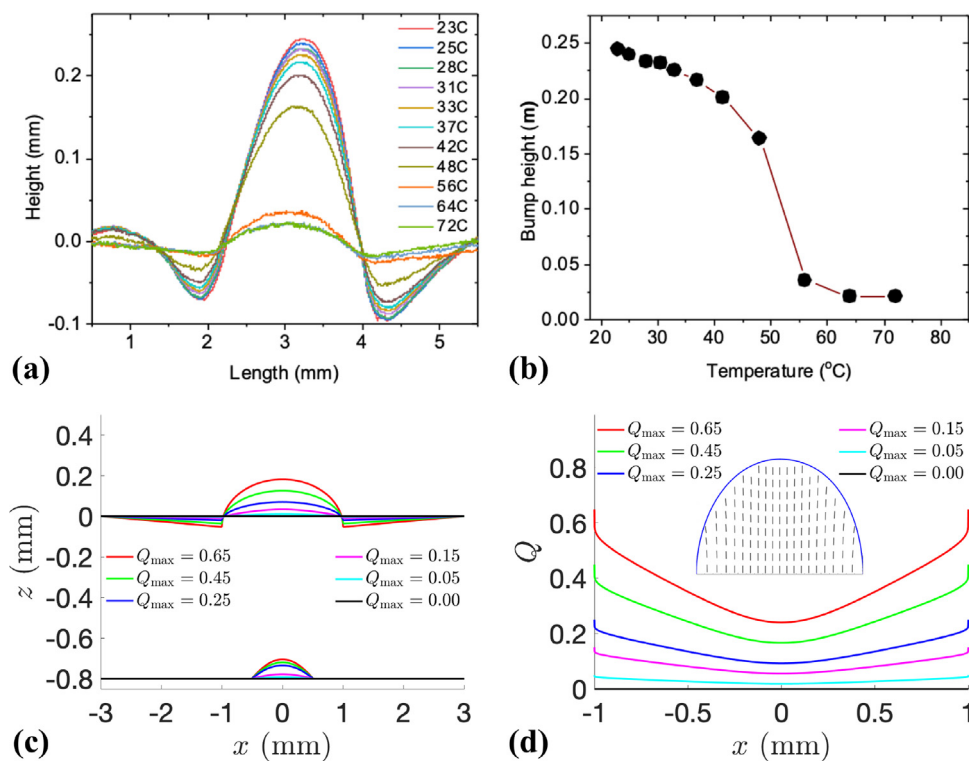
Fig. 4. (a) A sequence of profilometer scans of the top surface, as in Fig. 1(c), at different temperatures; (b) The summary of the peak height, measured from the profilometer scans against temperature, illustrating the (fully reversible) flattening of the bulge in the isotropic phase; (c) A sequence of analytical deformation profiles of the load-free system for different values of Q_{max}, reflecting temperature changes; (d) The corresponding local map of the induced order parameter $Q(x)$ for different values of Q_{max} in the bulge, with the inset showing the vertical director orientation.

reordering, that can be 'recorded' by second cross-linking, and then 'remembered' after the load is removed and a nematic phase is induced by varying temperature. Theoretically, this process can be modeled by considering both the elastic response of the matrix and the anelastic response of the embedded mesogens. The mathematical and numerical solutions of this model correctly capture all morphological features of the system and provide a full description of its mechanical behavior. The loaded system and its load-free actuation are mathematically tractable and experimentally controllable, rendering this process predictable for technological applications, such as controlling flows in a channel by blocking it or actuating textured surfaces.

CRediT authorship contribution statement

L. Angela Mihai: Conceived the idea, Discussed the main concepts, Developed the theoretical model and its implementation, Analyzed the data, Discussed the model, Wrote the paper. **Alexandra Gablier:** Conceived the idea, Discussed the main concepts, Carried out the experiments, Analyzed the data, Discussed the model, Wrote the paper. **Eugene M. Terentjev:** Conceived the idea, Discussed the main concepts, Analyzed the data, Discussed the model, Wrote the paper. **Alain Goriely:** Conceived the idea, Discussed the main concepts, Developed the theoretical model and its implementation, Analyzed the data, Discussed the model, Wrote the paper.

Declaration of competing interest

We, the authors of this paper, hereby declare that there is no conflict of interest concerning our research, findings, and publication of this work. We confirm that we have not been involved in any personal or financial relationships that could potentially be construed as influencing the content, methodology, or conclusions of our research.

Data availability

Data will be made available on request.

References

[1] M. Warner, E.M. Terentjev, Liquid Crystal Elastomers, Oxford University Press, New York, 2007.
[2] T.J. White, D.J. Broer, Programmable and adaptive mechanics with liquid crystal polymer networks and elastomers, Nature Mater. 14 (2015) 1087–1098.
[3] A. Gablier, E.M. Terentjev, Flexible force-bearing liquid crystalline elastomer component towards a dynamic braille platform, Nano Select 4 (2023) 1087–1098.
[4] K.L. Johnson, Contact Mechanics, Cambridge University Press, Cambridge, UK, 1985.
[5] AS Maghsoodi, M.O. Saed, E.M. Terentjev, K. Bhattacharya, Softening of the hertz indentation contact in nematic elastomers, Extreme Mech. Lett. 63 (2023) 102060.
[6] J. Weickenmeier, E. Kuhl, A. Goriely, The mechanics of decompressive craniectomy: Bulging in idealized geometries, J. Mech. Phys. Sol. 96 (2016) 572–590.
[7] A. Goriely, J. Weickenmeier, E. Kuhl, Stress singularities in swelling soft solids, Phys. Rev. Lett. 117 (2017) 138001.
[8] F. Benoist, F. Box, A. Goriely, Edge effects in elastic bulging, Int. J. Non-Linear Mech. 106 (2018) 227–237.
[9] S. Clarke, E. Terentjev, I. Kundler, H. Finkelmann, Texture evolution during the polydomain-monodomain transition in nematic elastomers, Macromolecules 31 (1998) 4862–4872.

[10] S.V. Fridrikh, E.M. Terentjev, Order–disorder transition in an external field in random ferromagnets and nematic elastomers, Phys. Rev. Lett. 79 (1997) 4661–4665.

[11] J.S. Biggins, M. Warner, K. Bhattacharya, Supersoft elasticity in polydomain nematic elastomers, Phys. Rev. Lett. 104 (2009) 037802.

[12] J.S. Biggins, M. Warner, K. Bhattacharya, Elasticity of polydomain liquid crystal elastomers, J. Mech. Phys. Sol. 60 (2012) 573–590.

[13] J. Kupfer, H. Finkelmann, Nematic liquid single crystal elastomers, Makromol. Chem. Rapid Commun. 12 (1991) 717–726.

[14] S.M. Clarke, E.M. Terentjev, I. Kundler, H. Finkelmann, Texture evolution during the polydomain-monodomain transition in nematic elastomers, Macromolecules 31 (1998) 4862–4872.

[15] S.V. Fridrikh, E.M. Terentjev, Polydomain-monodomain transition in nematic elastomers, Phys. Rev. E 60 (1999) 1847–1857.

[16] C.M. Yakacki, M.O. Saed, D.P. Nair, T. Gong, S.M. Reed, C.N. Bowman, Tailorable and programmable liquid-crystalline elastomers using a two-stage thiol–acrylate reaction, RSC Adv. 5 (2015) 18997–19001.

[17] M.O. Saed, A.H. Torbati, C.A. Starr, R. Visvanathan, N.A. Clark, C.M. Yakacki, Thiol-acrylate main-chain liquid-crystalline elastomers with tunable thermomechanical properties and actuation strain, J. Polym. Sci. B 55 (2017) 157–168.

[18] Y. Zhang, Z. Wang, Y. Yang, Q. Chen, X. Qian, Y. Wu, H. Liang, Y. Xu, Y. Wei, Y. Ji, Seamless multimaterial 3D liquid-crystalline elastomer actuators for next-generation entirely soft robots, Sci. Adv. 6 (2020) eaay8606.

[19] S. Kutter, E.M. Terentjev, Tube model for the elasticity of entangled nematic rubbers, Euro. Phys. J. E 6 (2001) 221–229.

[20] G. Feio, J.L. Figueirinhas, A.R. Tajbakhsh, E.M. Terentjev, Critical fluctuations and random-anisotropy glass transition in nematic elastomers, Phys. Rev. B. 78 (2008) 020201R.

[21] A. Hotta, E. Terentjev, Long-time stress relaxation in polyacrylate nematic liquid crystalline elastomers, J. Phys.: Condens. Matter 13, 11453–11464.

[22] A. Goriely, The Mathematics and Mechanics of Biological Growth, Springer-Verlag, New York, 2017.

[23] A. DeSimone, L. Teresi, Elastic energies for nematic elastomers, Euro. Phys. J. E Soft Matter 29 (2009) 191–204.

[24] L.A. Mihai, A. Goriely, A pseudo-anelastic model for stress softening in liquid crystal elastomers, Proc. R. Soc. Lond. Ser. A Math. Phys. Eng. Sci. 476 (2020) 20200558.

[25] H. Finkelmann, A. Greve, M. Warner, The elastic anisotropy of nematic elastomers, Euro. Phys. J. E Soft Mattert 5 (2001) 281–293.

[26] L.A. Mihai, A. Goriel, How to characterise a nonlinear elastic material? A review on nonlinear constitutive parameters in isotropic finite elasticity, Proc. Roy Soc. A 473 (2017) 20170607.